Double-Spiral Hexagonal Boron Nitride and Shear Strained Coalescence Boundary

Hyo Ju Park[1,2†], Roland Yingjie Tay[3†], Xiao Wang[2], Wen Zhao[2], Jung Hwa Kim[1], Rodney S. Ruoff[1,2,4], Feng Ding[1,2], Edwin Hang Tong Teo[3,5*], Zonghoon Lee[1,2*]

[1] School of Materials Science and Engineering, Ulsan National Institute of Science and Technology (UNIST), Ulsan 44919, Republic of Korea

[2] Center for Multidimensional Carbon Materials, Institute for Basic Science (IBS), Ulsan 44919, Republic of Korea

[3] School of Electrical and Electronic Engineering, Nanyang Technological University, 50 Nanyang Avenue, Singapore 639798, Singapore

[4] Department of Chemistry, Ulsan National Institute of Science and Technology (UNIST), Ulsan 44919, Republic of Korea

[5] School of Materials Science and Engineering, Nanyang Technological University, 50 Nanyang Avenue, Singapore 639798, Singapore

[†]These authors are equal major contributors to this work.

*e-mail: zhlee@unist.ac.kr; htteo@ntu.edu.sg

ABSTRACT

Among the different growth mechanisms for two-dimensional (2D) hexagonal boron nitride (h-BN) synthesized using chemical vapor deposition, spiraling growth of h-BN has not been reported. Here we report the formation of intertwined double-spiral few-layer h-BN that are driven by screw-dislocations located at the anti-phase boundaries of monolayer domains. The microstructure and stacking configurations were studied using a combination of dark-field and atomic-resolution transmission electron microscopy. Distinct from other 2D materials with single-spiral structures, the double-spiral structure enables the intertwined h-BN layers to preserve the most stable AA′ stacking configuration. We also found that the occurrence of shear strains at the boundaries of merged spiral islands is dependent on the propagation directions of encountering screw dislocations, and presented the strained features by density functional theory calculations and atomic image simulations. This study unveils the double-spiral growth of 2D h-BN multilayers and the creation of shear strain band at the coalescence boundary of two h-BN spiral clusters.

KEY WORDS: hexagonal boron nitride, growth mechanism, double-spiral, shear strain band, atmospheric pressure chemical vapor deposition

Introduction

Hexagonal boron nitride (h-BN) is analogous to graphene but is comprised of alternating boron and nitrogen atoms. It shows great potential as a substrate for two-dimensional (2D) heterostructured devices because of its atomically flat surface, unique electrically insulating nature, and high-temperature and chemical stability[1,2]. Using h-BN as a substrate layer for graphene increases the electron mobility by nearly an order of magnitude compared to conventional SiO_2 substrates[1]. Thus, h-BN has emerged as a critical building block for 2D heterostructured devices in which h-BN serves as a substrate, electron barrier, or passivation material[3-5]. The controllable and large-scale synthesis of h-BN films for use in scalable electronic devices has been achieved using chemical vapor deposition (CVD) on various catalytic metals[6-9]. Among metal substrates, Cu is most commonly used because of its abundance and its closely matched lattice constant with h-BN that enables epitaxial growth, resulting in relatively high-quality films[10,11]. It also facilitates h-BN growth by catalyzing the decomposition of BN precursors[12,13]. Furthermore, the relatively low solubilities of B and N in Cu allow a more controllable surface-mediated growth[8]. Planar and lateral growth has been observed in many studies for the first layer of h-BN[8,14,15]. A monolayer domain then nucleates on the Cu surface and grows laterally by the attachment of BN atoms to its edges. Following the Wulff construction, the resulting 2D single crystals often adopt well-defined shapes, e.g., triangles[8,15] and hexagons[14,16], depending on the edge attachment energies and the chemical potentials of the constituent elements[17-19].

As reported in previous studies, including our past research, the growth of h-BN does not cease after the formation of a monolayer[8,16]. However, a complete study of the growth mechanisms of multilayer h-BN films has not yet been made. Only a few studies have

discussed further growth processes. In one of the first studies on monolayer h-BN grown on Cu, Kim et al. reported that the growth was not self-limited and multilayer islands were observed after extended growth periods[8]. They concluded that the growth mechanism changed to the Stranki–Krastanov model (island on layer) after the completion of the first layer. In contrast, based on the in situ observation of Cu lattice expansion during h-BN growth, Kidambi et al. proposed that the second h-BN layer grows beneath the first layer in an inverted wedding cake structure formed by the incorporation of B atoms into bulk Cu[20]. Ji et al. grew few-layer h-BN domains and proposed that the growth of the subsequent layers originated from the same nucleation center as the monolayer domain thereby suggesting that growth of multilayers may be caused by defects[21], similar to previous reports on graphene adlayers[22-25].

Here we show that multilayer h-BN islands can also be formed from screw dislocations at anti-phase boundaries (APB)[26-28]. Unlike the single-spiral screw dislocation-driven growth in nanoplates and other 2D materials[29-33], a pair of screw dislocations always exist along an h-BN APB resulting in a double-spiral structure for isolated islands. Strained boundaries, a consequence of merged adjacent multilayer islands when the screw dislocations propagate in opposite directions, were commonly observed. Using a combination of transmission electron microscopy (TEM) and density functional theory (DFT) calculations, we propose what are the most stable strained features such as band width, magnitude, and direction between spiral clusters at the atomic scale.

Results

Synthesis and characterization of double-spiral h-BN.

Self-aligned monolayer h-BN films with multilayer islands were grown on resolidified Cu by atmospheric pressure (AP) CVD (refer to the Materials and Methods section). In the scanning electron microscopy image shown in Figure 1a, hexagonal multilayer islands are easily distinguished by their bright contrast. Multilayer islands tend to grow along defect lines (white lines in Figure 1a) with some as isolated individual islands while others are clustered and merged. The microstructures of these multilayer islands were elucidated using dark-field (DF) and atomic-resolution (AR) TEM. The DF-TEM image in Figure 1b reveals all the hexagonal multilayer islands grown along the defect lines are spiral-shape islands; an isolated multilayer island has a double-spiral structure while more complex spiral structures are formed when multiple islands are situated close together and merge along the defect lines. The one set of hexagonal diffraction spots (inset of Figure 1b) indicates that all the monolayer h-BN domains and multilayers in Figure 1b share the same orientation. While, the spiral contours of the multilayer islands are divided by defect lines, which means these defect lines are APBs that are created where two monolayer domains having different polarities, i.e. BN/NB (60 ° rotation angle difference), meet (see Figure S1). In a previous study[16], we demonstrated that h-BN monolayer single crystals grown by CVD primarily have the same orientation and comprise both BN and NB domains, with defect lines along the APBs. Also note that the isolated spiral islands tend to be bigger in lateral size (~1 μm) than clustered ones (see the Figure 1a and Figure S1a) and their hexagonal edges are usually aligned to the zigzag direction as verified by the orientation of diffraction pattern (inset of Figure 1b). This indicates the presence of alternating B- and N-terminated edges[14]. Whereas, clustered spiral islands show slightly mixed

edges where they merge. Both left- and right-handed spirals were observed and found up to 7 layers as far as we have searched.

Figure 1c shows an AR-TEM image at the interlayer boundary region of a double-spiral multilayer island as indicated by the red box in Figure 1b. The number of h-BN layers was determined by etching the layers by prolonged electron-beam irradiation. The left and right regions were determined to be two and three layers respectively, confirming that the number of h-BN layers increases by one for each rotation. The interlayer boundary was identified from the intensity profile (Figure 1d) across the blue line shown in the AR-TEM image in Figure 1c. Fast Fourier transforms (FFTs) of the bilayer and trilayer regions (insets in Figure 1c) indicate the same hexagonal structure with no difference in orientation. The layer boundary has zigzag termination as suggested earlier in Figure 1b that spiral islands grow along the zigzag direction. The stacking structure was evaluated from the orientation of the triangular defects created by electron beam irradiation. Since the triangular hole defects of h-BN have N-terminated edges [34-36], the opposite orientation of the triangular defects between adjacent layers indicates that the h-BN layers were AA′-stacked (i.e., BN/NB/BN/NB; Figure 1e), which is the most energetically favorable stacking configuration in bulk h-BN[37,38]. More than one hundred locations on many different islands synthesized from different batches were inspected to have AA′ stacking structure, judged by the atomic lattice, FFT, and orientations of triangular defects in adjacent layers at atomic resolution. Moreover, DF-TEM images acquired from first- and second-order diffraction spot showed increasing contrast with the number of layers as shown in Figure 1b, which means the whole double-spiral structure has AA′ stacking[39]. The above analyses suggest that the double-spiral multilayer island was formed with AA′ stacking with

two intertwined h-BN domains, which spiral around each other one layer per step across the APB.

Growth mechanism of screw dislocation-driven double-spiral h-BN.

Based on the results of TEM characterization in Figure 1, we inferred the mechanism for the double-spiral growth of isolated multilayer islands. Figure 2a shows a false-colored DF-TEM image of an isolated double-spiral multilayer h-BN island which is schematically depicted in Figure 2b showing the layer numbers and the domain orientations. The formation mechanism of double-spiral h-BN multilayers is illustrated in Figure 2c. At first, monolayer domains nucleate and then grow epitaxially along the (110) Cu surface by edge attachment (EBSD shows that the resolidified Cu has a surface orientation of (110)). Because of the prolific nucleation of h-BN, there are numerous instances where the edges of neighboring domains meet. If domains coalescence with the same polarity (BN/BN), they can stitch seamlessly together, while those with different polarities (BN/NB) cannot, leaving exposed edges and an APB instead. When the APCVD growth of h-BN continues after the monolayer has fully covered the Cu surface, an abundance of multilayer h-BN spiraling islands is formed along the APBs, where a pair of dislocations is initiated and causes the h-BN domains to simultaneously grow and extend over each other. Growth progressed by spiraling in the vertical direction as the BN atoms attached to the active edges, leaving slipped planes in the bottom layer (i.e., generating screw defects). Once each spiral reached the domain boundary, another layer grew on top of the existing one. This process continued perpetually. TEM observations have shown that the spirals climbed one layer per step, which is equivalent to one elemental Burgers vector of h-BN. Because the top layer was the last to form and had the least time to grow, the multilayer islands formed pyramid-like structures in which the layers became progressively

smaller while moving toward the top (Figure 2d and Movie S1). Each of the two spiraling domains grew independently across the boundary and retained its orientation, thereby maintaining the energetically favorable AA′ stacking at each side of domains to the APB. This is possible because of the double-spiral system, which was initiated at the APB. The single-spiral driven by a single screw dislocation observed in other 2D materials including graphene[29], molybdenum disulfide[30,31], and tungsten diselenide[32] showed AA-like stacking configurations (which means AA, or AB, or with translation but not twisted in-between layers), because the crystal orientation remained unchanged. Whereas, double-spirals, recently reported in metal dichalcogenide materials, were also observed to have AA′-like stacking configuration with 60 ° or 180 ° rotation of one layer from the other[40,41]. Notable thing is that the h-BN double-spirals are always grown intertwined, driven by paired screw-dislocations at the APB, while the initiation of screw-dislocations can be independent and merging of two single-spiral results in double-spiral in metal dichalcogenide materials reported so far.

Furthermore, we verified the spiral islands grow upward from the initial monolayer by spiraling around the axial dislocation located at the APB as BN atoms are attached to the active edges, as illustrated in Figure 2d. It is experimentally demonstrated by comparing the orientations of triangular defects on layer boundary in Figure S2 (refer to the section 1 in the Supporting Information). Therefore, unlike bottom growth caused by the substrate’s catalytic effect, which results in the “inverted wedding cake” structure and is commonly found in few-layer graphene[22-25], growth by screw dislocations occurs by a top growth mechanism in which the growth extends from the first layer and spirals upward around an axial dislocation, forming multiple layers of perpetuating steps, which agree to our recent study of spiral growth in graphene[42].

Shear strain band at coalescence boundary of h-BN spiral clusters.

Typically, h-BN spiral islands cluster along defect lines as a result of the many screw dislocation sites situated along the APBs (Figure 1a). Interestingly, these clusters exhibited different features, as observed in the DF-TEM images in Figure 3a,b. Some clusters were smoothly connected (Figure 3a), whereas others showed dark lines in between merged multilayer regions (Figure 3b). The DF-TEM images in both Figure 3a and b were acquired by selecting a second-order diffraction spot in the selected area electron diffraction pattern. This should result in increased intensity of the DF-TEM image with increasing number of layers when the layers are well ordered without misorientation (AA′-stacked) by constructive interference of waves between layers[43,44]. Hence, the dark lines in Figure 3b indicate strained regions that have lost the high-symmetry stacking configuration (not AA′-stacked). The absence or presence of these dark lines in Figure 3a,b are related to the rotation direction of neighboring islands. When two neighboring islands grow in opposite spiraling directions (i.e., one left-handed and one right-handed), they coalesce smoothly because the encountering screw dislocations propagate in the same direction (Figure 3c). However, when they have the same spiraling direction (i.e., both are right- or left- handed spirals), the counter-directional propagation of screw dislocations at the merging region results in a strained boundary between them (Figure 3d), from the APB to merging apex.

The regions with dark lines were further investigated at in the TEM at the atomic scale. An AR-TEM image of the white rectangular area including a dark line in Figure 4a is shown in

Figure 4b. A strained region along the zigzag direction was observed, as indicated by the red dashed lines. The FFT (inset of Figure 4b) shows only one set of hexagonal diffraction spots, indicating that the strained structure was caused by a gradual shift in the relative atomic position between layers with no interlayer twisting[45]. Figure 4c shows a magnified atomic resolution image within the area indicated by a cyan rectangle in Figure 4b. The square pattern observed in the center of Figure 4c gradually becomes 'wiggly' moving away from the center before returning to the stable hexagonal configuration. By fitting the atomic models with different widths and magnitude of the shear strain (Figure S3 and Figure S4), we replicated the experimental dimensions of the strained region using a shear strain magnitude of 1 unit cell of h-BN (2.50 Å) on the upper layer of AA′-stacked bilayer h-BN, with a width of approximately 10 nm along the zigzag direction (Figure 4d). The simulated TEM image shown in Figure 4e closely resembles the experimental image. The shear strain band had a width of approximately 10 nm (including approximately 2 nm of square patterns, 4 nm of wiggly patterns, and 4 nm of slightly misfit hexagonal patterns), consistent with the width of the dark lines observed in the DF-TEM image (Figure 4a). To obtain the general value of shear strain in an h-BN spiral, we calculated the total increase in energy for the shear of a 1 h-BN unit cell in AA′-stacked h-BN. Shear strain increases the total energy by both elastic deformation (ΔE_{ED}) and turbostratic stacking, reducing the van der Waals (vdW) interaction between layers (ΔE_{vdW}):

$$\Delta E_{total} = \Delta E_{ED} + \Delta E_{vdW}. \qquad (1)$$

ΔE_{total} can be rewritten as follows:

$$\Delta E_{total} = G \times a^3 \times h/b + \alpha \times a \times b, \qquad (2)$$

where G is the shear modulus, α is the scaling factor (α = the reduction in vdW energy per area), a is the displacement of h-BN along the zigzag direction, b is the width of the shear region in the armchair direction, and h is the layer distance in h-BN (refer to Supporting Information for the derivation of the equations). Based on Eq. (2), the total increase in the energy attributed to the shear strain can be obtained from b, i.e., the width of the shear strain band (Figure 4f). The width of the shear strain band corresponds to the local minimum in total energy and was calculated to be 9.56 nm, which is in agreement with the experimental results and image simulation model (Figure 4 d,e). This explains why many of the observed dark lines had similar widths (9–10 nm). Thus, the merging of h-BN spiral islands grown from counter-directional screw dislocations induces a shear strain over a distance of 9.56 nm between the islands, generating moiré patterns in the AR-TEM image and dark lines in the DF-TEM image. Strained h-BN was reported to have different characteristics to pristine h-BN, for example, causing phonon shift[46]. This study on the formation conditions of shear strain may give an insight for the use of strained h-BN in electronic devices, 2D heterostructures, and especially as a platform for tuning the electronic structure of graphene[47].

Discussion

In this study, growth was carried out at atmospheric pressure with 200:5 sccm of $Ar:H_2$ flow, potentially leading to the overgrowth at the exposed edges of APBs. Since the gas flow rate is higher to LPCVD, there are more collisions between the gas molecules/precursor leading to more active precursor species to be absorbed at the exposed edges of APBs. Furthermore, the growth was controlled by feeding small amounts of precursor (8 mg of ammonia borane heated

at 85 °C) to the system, fostering low supersaturation conditions which enable the growth of multilayers by screw dislocation. According to the Burton–Cabrera–Frank theory, crystal growth is dominated by dislocations at low supersaturation condition[48-50]. And dislocations are also known to form along the grain boundaries of merged monolayer domains[51], especially APBs of aligned h-BN domains in our case. Therefore, the spiral growth extends from the first layer as the BN atoms attached to the active edges of APBs, and grow upward spiraling around the axial dislocation in the vertical direction.

In summary, multilayered h-BN spiral islands were grown along the APBs of aligned h-BN on resolidified Cu substrates by APCVD at low supersaturation condition. Paired screw-dislocations initiated at the APBs resulted in intertwined spiraling h-BN domains which climb one layer per step across the APB by growing from the active edges. The double-spiral structure means that the h-BN multilayer preserves AA′ stacking configuration throughout the entire region unlike other 2D materials with a single spiral structure. The shear strain bands along the boundaries between merged multilayer regions were commonly observed arising from neighboring islands with counter-directional screw dislocations. The strained regions, which are typically 9-10 nm wide, generate moiré patterns at the coalescence boundaries between adjacent multilayer spirals. This study provides understanding of the growth of double-spiral h-BN multilayers and explains the shear strain between h-BN spiral clusters.

Materials and Methods

Synthesis of multilayer h-BN spirals. h-BN was grown on resolidified Cu by CVD at atmospheric pressure, as reported previously[16]. W foil (Alfa Asear; product no. 10417;

thickness = 50 μm) was used as a supporting substrate for the Cu. Three pieces of Cu foil (Alfa Asear; product no. 13382; thickness = 25 μm) were cut to 2 cm × 1.5 cm and placed on top of the W foil. The stack was then loaded into a 1-inch quartz tube. The temperature of the furnace was first increased to 1000°C in 50 min and then to 1090°C in 10 min under a constant Ar/H_2 flow (200:5 sccm). Subsequently, the temperature was maintained at 1090°C for 30 min and then gradually decreased to 1075°C at a rate of 1°C/min. For h-BN growth, ~8 mg of ammonia borane (Sigma Aldrich, 97%) was placed in a ceramic boat upstream of the heating zone and heated at ~85°C using a heating belt for 30 min. After the growth, the temperature was quickly decreased by opening the lid of the furnace.

TEM characterization of the h-BN spiral structure. CVD-grown multilayer h-BN was directly transferred onto a TEM grid[52]. TEM analysis was conducted on an aberration-corrected transmission electron microscope (FEI Titan3 G2 60-300) operated at 80 kV. Atomic resolution was successfully obtained at −21 μm ± 0.5 μm of spherical aberration (C_s) using a monochromator. The AR-TEM images were acquired with an exposure time of 0.2 s and an electron dose of approximately 5×10^5 e^- nm^{-2}. The DF-TEM images were taken from a second-order diffraction spot to identify the multilayer structures because the intensity of the SAED and DF-TEM images improves with increasing number of layers when multilayers are stacked with high symmetry such as AA′ or AB stacking[43,44]. An objective aperture with a radius of 1.28 nm^{-1} was placed on the back focal plane of the diffraction spots to collect electrons diffracted from the crystallographic plane of interest.

TEM image processing and simulations. For better visualization, some DF-TEM images were colorized by a lookup table using ImageJ. TEM image simulation was implemented in MacTempasX under experimental imaging conditions.

Computational modeling. The DFT-based calculations within the Vienna Ab initio Simulation Package (VASP)[53,54] were performed to optimize the AA′-stacked h-BN. The electronic exchange and correlation were described by the Perdew–Burke–Ernzerhof[55] functional in the generalized gradient approximation. The interaction between the valence electrons and ion cores was embodied in the projected augmented-wave method[56,57] with a cutoff energy of 400 eV. The Grimme DFT-D2 method[58] was used to modify the contribution of interlayer interactions. A supercell volume of $2.50 \times 108.40 \times 20.00$ Å^3 made the vacuum space sufficiently large to void image interference. Accordingly, $9\times1\times1$ k-points were uniformly sampled in the Brillouin zone using the Monkhorst–Pack method[59] to ensure an energy convergence of less than 0.1 meV/atom. For simplification, the following optimizations and deductions are based on bilayer h-BN: the bottom layer was fixed, and a uniformly distributed shear was imposed along the zigzag direction on the top layer. This is in accordance with the experimental observations. The shortest dislocation length along the zigzag direction was one periodic unit (i.e., 2.50 Å). All structures were optimized using the conjugate gradient algorithm until the convergence reached 0.01 eV/Å.

ASSOCIATED CONTENT

Supporting Information. Additional information on growth direction and calculation of shear model, Figures S1-S7, Table S1 and Movie S1.

AUTHOR INFORMATION

Corresponding Author

*e-mail: zhlee@unist.ac.kr; htteo@ntu.edu.sg

Notes

The authors declare no competing financial interests

Acknowledgments

This work was supported by IBS-R019-D1, the National Research Foundation (NRF) grant funded by the Korea government (MSIT) (No. 2018R1A2A2A05019598), and the NRF-ANR Joint Grant number NRF2016-NRF-ANR001.

References

1. Dean, C. R.; Young, A. F.; Meric, I.; Lee, C.; Wang, L.; Sorgenfrei, S.; Watanabe, K.; Taniguchi, T.; Kim, P.; Shepard, K. L.; Hone, J. *Nature Nanotechnology* **2010,** 5, (10), 722-6.

2. Liu, Z.; Gong, Y.; Zhou, W.; Ma, L.; Yu, J.; Idrobo, J. C.; Jung, J.; MacDonald, A. H.; Vajtai, R.; Lou, J.; Ajayan, P. M. *Nat Commun* **2013,** 4.

3. Geim, A. K.; Grigorieva, I. V. *Nature* **2013,** 499, (7459), 419-425.

4. Britnell, L.; Gorbachev, R. V.; Jalil, R.; Belle, B. D.; Schedin, F.; Mishchenko, A.; Georgiou, T.; Katsnelson, M. I.; Eaves, L.; Morozov, S. V.; Peres, N. M. R.; Leist, J.; Geim, A. K.; Novoselov, K. S.; Ponomarenko, L. A. *Science* **2012,** 335, (6071), 947-50.

5. Avsar, A.; Vera-Marun, I. J.; Tan, J. Y.; Watanabe, K.; Taniguchi, T.; Castro Neto, A. H.; Özyilmaz, B. *ACS Nano* **2015,** 9, (4), 4138-4145.

6. Song, L.; Ci, L.; Lu, H.; Sorokin, P. B.; Jin, C.; Ni, J.; Kvashnin, A. G.; Kvashnin, D. G.; Lou, J.; Yakobson, B. I.; Ajayan, P. M. *Nano Letters* **2010,** 10, (8), 3209-3215.

7. Shi, Y.; Hamsen, C.; Jia, X.; Kim, K. K.; Reina, A.; Hofmann, M.; Hsu, A. L.; Zhang, K.; Li, H.; Juang, Z.-Y.; Dresselhaus, M. S.; Li, L.-J.; Kong, J. *Nano Letters* **2010,** 10, (10), 4134-4139.

8. Kim, K. K.; Hsu, A.; Jia, X.; Kim, S. M.; Shi, Y.; Hofmann, M.; Nezich, D.; Rodriguez-Nieva, J. F.; Dresselhaus, M.; Palacios, T.; Kong, J. *Nano Letters* **2012,** 12, (1), 161-166.

9. Kim, G.; Jang, A. R.; Jeong, H. Y.; Lee, Z.; Kang, D. J.; Shin, H. S. *Nano Letters* **2013,** 13, (4), 1834-1839.

10. Liu, L.; Siegel, D. A.; Chen, W.; Liu, P.; Guo, J.; Duscher, G.; Zhao, C.; Wang, H.; Wang, W.; Bai, X.; McCarty, K. F.; Zhang, Z.; Gu, G. *Proceedings of the National Academy of Sciences* **2014,** 111, (47), 16670-16675.

11. Wood, G. E.; Marsden, A. J.; Mudd, J. J.; Walker, M.; Asensio, M.; Avila, J.; Chen, K.; Bell, G. R.; Wilson, N. R. *2D Materials* **2015,** 2, (2), 025003.

12. Frueh, S.; Kellett, R.; Mallery, C.; Molter, T.; Willis, W. S.; King'ondu, C.; Suib, S. L. *Inorg Chem* **2011,** 50, (3), 783-792.

13. Lu, G. Y.; Wu, T. R.; Yuan, Q. H.; Wang, H. S.; Wang, H. M.; Ding, F.; Xie, X. M.; Jiang, M. H. *Nat Commun* **2015,** 6.

14. Tay, R. Y.; Griep, M. H.; Mallick, G.; Tsang, S. H.; Singh, R. S.; Tumlin, T.; Teo, E. H. T.; Karna, S. P. *Nano Letters* **2014,** 14, (2), 839-846.

15. Wang, L.; Wu, B.; Chen, J.; Liu, H.; Hu, P.; Liu, Y. *Advanced Materials* **2014,** 26, (10), 1559-1564.

16. Tay, R. Y.; Park, H. J.; Ryu, G. H.; Tan, D.; Tsang, S. H.; Li, H.; Liu, W.; Teo, E. H. T.; Lee, Z.; Lifshitz, Y.; Ruoff, R. S. *Nanoscale* **2016,** 8, (4), 2434-2444.

17. Liu, Y.; Bhowmick, S.; Yakobson, B. I. *Nano Letters* **2011,** 11, (8), 3113-3116.

18. Zhang, Z.; Liu, Y.; Yang, Y.; Yakobson, B. I. *Nano Letters* **2016,** 16, (2), 1398-1403.

19. Zhao, R.; Gao, J.; Liu, Z.; Ding, F. *Nanoscale* **2015,** 7, (21), 9723-9730.

20. Kidambi, P. R.; Blume, R.; Kling, J.; Wagner, J. B.; Baehtz, C.; Weatherup, R. S.; Schloegl, R.; Bayer, B. C.; Hofmann, S. *Chem. Mater.* **2014,** 26, (22), 6380-6392.

21. Ji, Y. X.; Calderon, B.; Han, Y. M.; Cueva, P.; Jungwirth, N. R.; Alsalman, H. A.; Hwang, J.; Fuchs, G. D.; Muller, D. A.; Spencer, M. G. *Acs Nano* **2017,** 11, (12), 12057-12066.

22. Shu, N.; Wei, W.; Shirui, X.; Qingkai, Y.; Jiming, B.; Shin-shem, P.; Kevin, F. M. *New. J. Phys.* **2012,** 14, (9), 093028.

23. Li, Q.; Chou, H.; Zhong, J.-H.; Liu, J.-Y.; Dolocan, A.; Zhang, J.; Zhou, Y.; Ruoff, R. S.; Chen, S.; Cai, W. *Nano Lett.* **2013,** 13, (2), 486-490.

24. Fang, W.; Hsu, A. L.; Caudillo, R.; Song, Y.; Birdwell, A. G.; Zakar, E.; Kalbac, M.; Dubey, M.; Palacios, T.; Dresselhaus, M. S.; Araujo, P. T.; Kong, J. *Nano Letters* **2013,** 13, (4), 1541-1548.

25. Hao, Y.; Wang, L.; Liu, Y.; Chen, H.; Wang, X.; Tan, C.; Nie, S.; Suk, J. W.; Jiang, T.; Liang, T.; Xiao, J.; Ye, W.; Dean, C. R.; Yakobson, B. I.; McCarty, K. F.; Kim, P.; Hone, J.; Colombo, L.; Ruoff, R. S. *Nat Nano* **2016,** 11, (5), 426-431.

26. van der Zande, A. M.; Huang, P. Y.; Chenet, D. A.; Berkelbach, T. C.; You, Y. M.; Lee, G. H.; Heinz, T. F.; Reichman, D. R.; Muller, D. A.; Hone, J. C. *Nat. Mater.* **2013,** 12, (6), 554-561.

27. Zhou, W.; Zou, X. L.; Najmaei, S.; Liu, Z.; Shi, Y. M.; Kong, J.; Lou, J.; Ajayan, P. M.; Yakobson, B. I.; Idrobo, J. C. *Nano Lett.* **2013,** 13, (6), 2615-2622.

28. Najmaei, S.; Liu, Z.; Zhou, W.; Zou, X. L.; Shi, G.; Lei, S. D.; Yakobson, B. I.; Idrobo, J. C.; Ajayan, P. M.; Lou, J. *Nat. Mater.* **2013,** 12, (8), 754-759.

29. Nicholas, N. W.; Connors, L. M.; Ding, F.; Yakobson, B. I.; Schmidt, H. K.; Hauge, R. H. *Nanotechnology* **2009,** 20, (24), 245607.

30. Ly, T. H.; Zhao, J.; Kim, H.; Han, G. H.; Nam, H.; Lee, Y. H. *Adv Mater* **2016,** 28, (35), 7723-8.

31. Zhang, L.; Liu, K.; Wong, A. B.; Kim, J.; Hong, X.; Liu, C.; Cao, T.; Louie, S. G.; Wang, F.; Yang, P. *Nano Letters* **2014,** 14, (11), 6418-6423.

32. Chen, L.; Liu, B.; Abbas, A. N.; Ma, Y.; Fang, X.; Liu, Y.; Zhou, C. *ACS Nano* **2014,** 8, (11), 11543-11551.

33. Sarma, P. V.; Patil, P. D.; Barman, P. K.; Kini, R. N.; Shaijumon, M. M. *RSC Advances* **2016,** 6, (1), 376-382.

34. Yin, L. C.; Cheng, H. M.; Saito, R. *Phys Rev B* **2010,** 81, (15).

35. Kotakoski, J.; Jin, C. H.; Lehtinen, O.; Suenaga, K.; Krasheninnikov, A. V. *Phys Rev B* **2010,** 82, (11).

36. Ryu, G. H.; Park, H. J.; Ryou, J.; Park, J.; Lee, J.; Kim, G.; Shin, H. S.; Bielawski, C. W.; Ruoff, R. S.; Hong, S.; Lee, Z. *Nanoscale* **2015,** 7, (24), 10600-10605.

37. Kern, G.; Kresse, G.; Hafner, J. *Phys. Rev. B.* **1999,** 59, (13), 8551-8559.

38. Pease, R. S. *Nature* **1950,** 165, (4201), 722-723.

39. Kim, C. J.; Brown, L.; Graham, M. W.; Hovden, R.; Havener, R. W.; McEuen, P. L.; Muller, D. A.; Park, J. *Nano Lett* **2013,** 13, (11), 5660-5665.

40. Fan, X. P.; Zhao, Y. Z.; Zheng, W. H.; Li, H. L.; Wu, X. P.; Hu, X. L.; Zhang, X. H.; Zhu, X. L.; Zhang, Q. L.; Wang, X.; Yang, B.; Chen, J. H.; Jin, S.; Pan, A. *Nano Lett* **2018,** 18, (6), 3885-3892.

41. Shearer, M. J.; Samad, L.; Zhang, Y.; Zhao, Y. Z.; Puretzky, A.; Eliceir, K. W.; Wright, J. C.; Hamers, R. J.; Jin, S. *J Am Chem Soc* **2017,** 139, (9), 3496-3504.

42. Tay, R. Y.; Park, H. J.; Ling, J. J.; Ng, Z. K.; Jing, L.; Li, H. L.; Zhu, M. M.; Tsang, S. H.; Lee, Z.; Teo, E. H. T. *Chem Mater* **2018,** 30, (19), 6858-6866.

43. Shevitski, B.; Mecklenburg, M.; Hubbard, W. A.; White, E. R.; Dawson, B.; Lodge, M. S.; Ishigami, M.; Regan, B. C. *Phys Rev B Condens Matter Mater Phys* **2013,** 87, 045417.

44. Ping, J.; Fuhrer, M. S. *Nano Lett* **2012,** 12, (9), 4635-41.

45. Lin, J.; Fang, W.; Zhou, W.; Lupini, A. R.; Idrobo, J. C.; Kong, J.; Pennycook, S. J.; Pantelides, S. T. *Nano Lett* **2013,** 13, (7), 3262-8.

46. Androulidakis, C.; Koukaras, E. N.; Poss, M.; Papagelis, K.; Galiotis, C.; Tawfick, S. *Phys Rev B* **2018,** 97, (24).

47. Khatibi, Z.; Namiranian, A.; Panahi, S. *Physica B: Condensed Matter* **2018**.

48. Markov, I. V., *Crystal growth for beginners : fundamentals of nucleation, crystal growth and epitaxy*. World Scientific: Singapore, 1994.

49. Burton, W. K.; Cabrera, N.; Frank, F. C. *Nature* **1949,** 163, 398-399.

50. Burton, W. K.; Cabrera, N.; Frank, F. C. *Philosophical Transactions of the Royal Society of London A: Mathematical, Physical and Engineering Sciences* **1951,** 243, (866), 299-358.

51. Huang, P. Y.; Ruiz-Vargas, C. S.; van der Zande, A. M.; Whitney, W. S.; Levendorf, M. P.; Kevek, J. W.; Garg, S.; Alden, J. S.; Hustedt, C. J.; Zhu, Y.; Park, J.; McEuen, P. L.; Muller, D. A. *Nature* **2011,** 469, (7330), 389-392.

52. Regan, W.; Alem, N.; Aleman, B.; Geng, B. S.; Girit, C.; Maserati, L.; Wang, F.; Crommie, M.; Zettl, A. *Appl Phys Lett* **2010,** 96, (11).

53. Kresse, G.; Furthmüller, J. *Computational Materials Science* **1996,** 6, (1), 15-50.

54. Kresse, G.; Furthmüller, J. *Phys Rev B* **1996,** 54, (16), 11169.

55. Perdew, J. P.; Burke, K.; Ernzerhof, M. *Physical review letters* **1996,** 77, (18), 3865.

56. Blöchl, P. E. *Phys Rev B* **1994,** 50, (24), 17953.

57. Kresse, G.; Joubert, D. *Phys Rev B* **1999,** 59, (3), 1758.

58. Grimme, S. *Journal of computational chemistry* **2006,** 27, (15), 1787-1799.

59. Monkhorst, H. J.; Pack, J. D. *Phys Rev B* **1976,** 13, (12), 5188.

60. This work is based on a part of the first author, H.J. Park's Ph. D. thesis at Ulsan National Institute of Science and Technology.

Figures

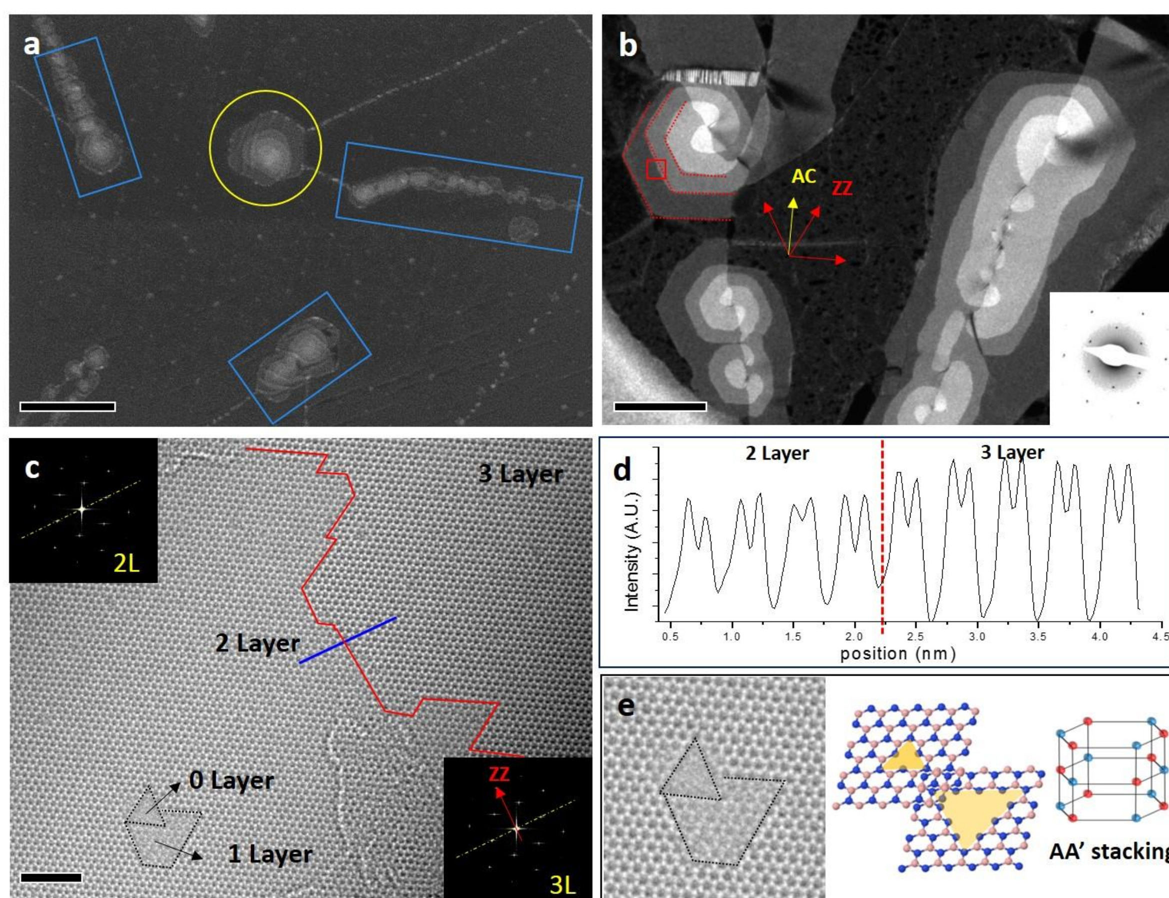

Figure 1. Spiral growth of multilayer h-BN islands. (a) SEM image of multilayer h-BN islands grown on a resolidified Cu substrate. Both isolated (yellow circle) and clustered (blue rectangles) spirals exist along defect lines in monolayer h-BN. (b) DF-TEM image showing the spiral structure of the h-BN islands. The islands have a double-spiral structure along the APB. The inset shows the SAED pattern of the entire area of (b). (c) AR-TEM image of the area indicated by the red square in (b). The red line indicates a layer boundary. Insets are the FFTs over the bi- and tri-layer regions. (d) Intensity profile along the blue line in (c). There is a one layer increase for each spiral contour. (e) The opposite direction of an electron beam-induced triangular hole defect in the neighboring layers demonstrates the AA′ stacking configuration of multilayer h-BN. Scale bars (a), 1 μm, (b), 0.2 μm, (c), 2 nm.

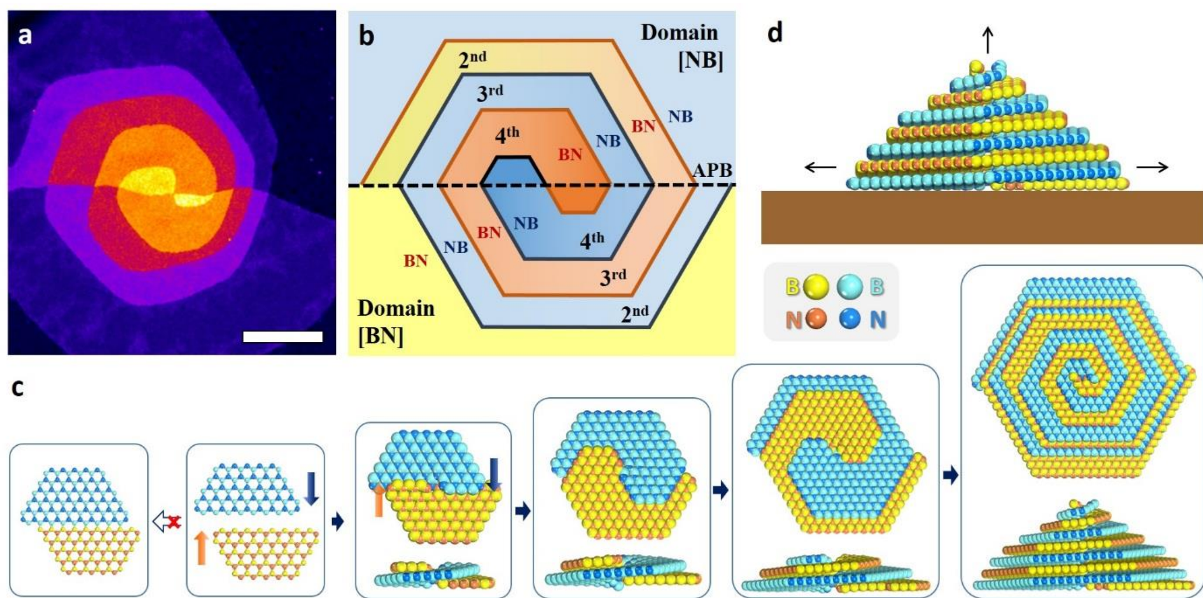

Figure 2. Growth mechanism of h-BN spirals. (a) False-colored DF-TEM image of multilayer h-BN with a double-spiral structure along the APB (scale bar, 0.2 μm). (b) Illustration of (a) with information of the number of layers and domain orientations. (c) Illustration of growth mechanism of h-BN spirals. (d) Side view of top growth of multilayer island from the substrate.

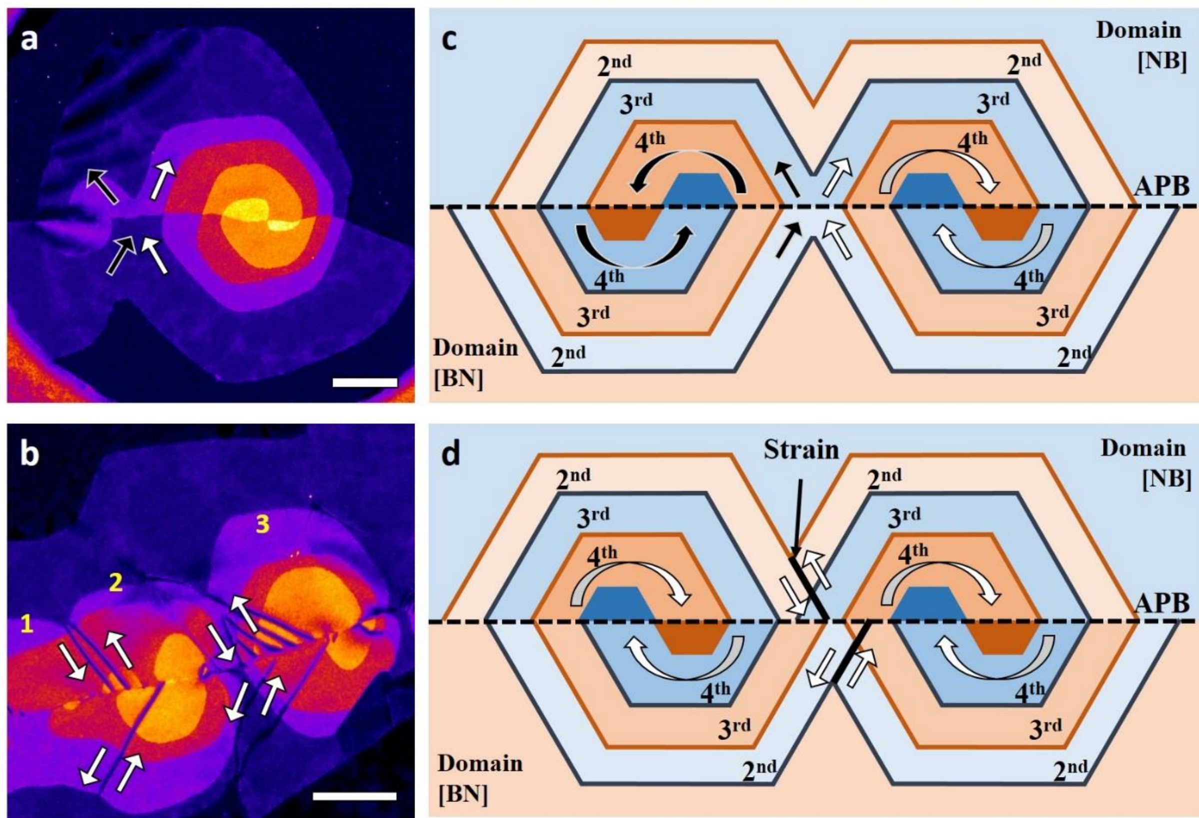

Figure 3. Merging of h-BN spirals and creation of strain. (a, b) False-colored DF-TEM images of spiral clusters. Two islands smoothly merge in (a), whereas dark lines are formed between the merging regions of three islands in (b). (c, d) Schematics showing the merging of two islands: (c) is for the case in (a), where the two spirals have opposite rotations (right- and left-handed spirals) and (d) is for the case in (b), where the two spirals have the same rotation (both left-handed). The right- and left-handed spirals are represented by black and white curved arrows, respectively, and the propagation directions of the screw dislocations are indicated by an arrow with the same color of the corresponding spiral direction. The black dashed lines are the APBs formed between the [NB] (blue) and [BN] (orange) domains. The solid black line indicates strain between the two merging spiral islands. Scale bars (a,b), 0.2 μm.

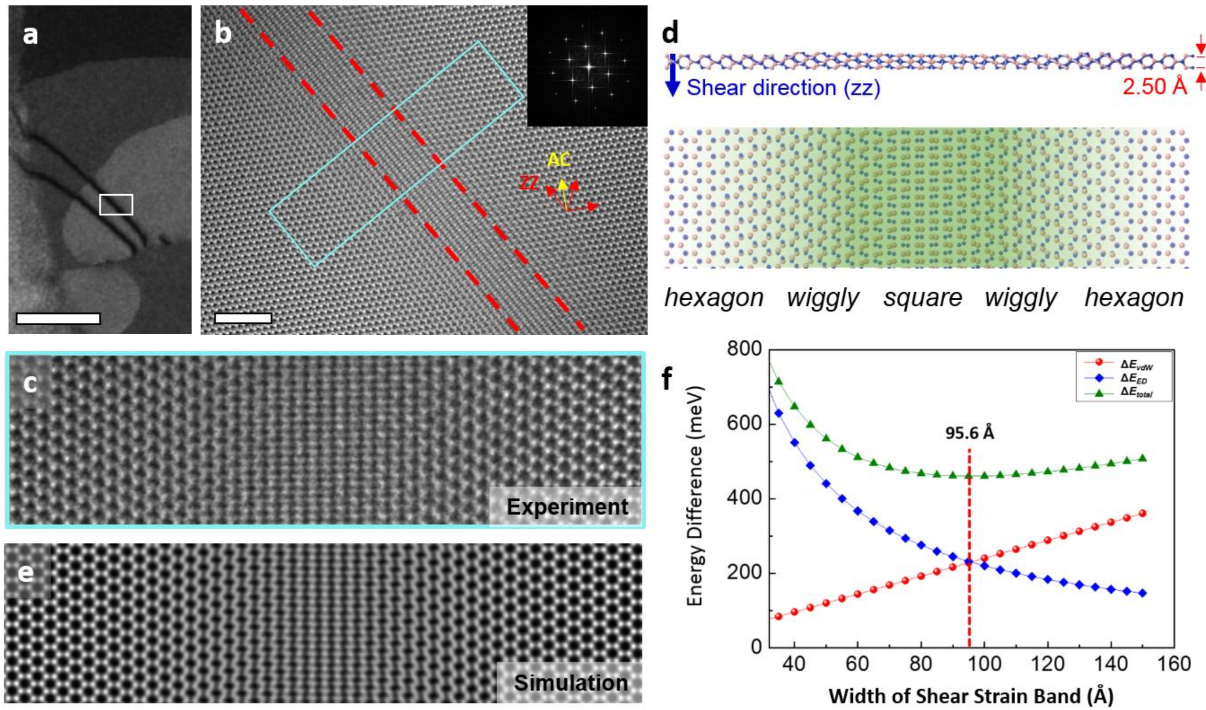

Figure 4. Shear strain band in h-BN spirals. (a) DF-TEM image of strained h-BN (strain indicated by dark lines). (b) AR-TEM image of the area indicated by the white box in (a). The inset shows the FFT over the whole area. The region highlighted by the red dashed lines along the zigzag direction shows a square-like moiré pattern instead of the original hexagonal lattice of h-BN with AA′ stacking configuration. (d) Magnified AR-TEM image of the boxed region with cyan color in (b). (d) Applying a 1 h-BN unit cell (2.50 Å) shear strain along the zigzag direction makes similar feature with (c), including hexagonal, wiggly, and square regions over a width of ~10 nm. (e) Simulated TEM image from the structure in (c). (f) The increase in total energy (ΔE_{total}) resulting from the shear strain depends on the width of the shear strain band. ΔE_{total} is minimized when the width of the shear strain band is 9.56 nm. Scale bars (a), 1 μm, (b), 2 nm.

Supporting Information

Double-Spiral Hexagonal Boron Nitride and Shear Strained Coalescence Boundary

Hyo Ju Park[1,2†], Roland Yingjie Tay[3,4†], Xiao Wang[2], Wen Zhao[2], Jung Hwa Kim[1], Rodney S. Ruoff[1,2,5], Feng Ding[1,2], Edwin Hang Tong Teo[3,6*], Zonghoon Lee[1,2*]

1 School of Materials Science and Engineering, Ulsan National Institute of Science and Technology (UNIST), Ulsan 44919, Republic of Korea

2 Center for Multidimensional Carbon Materials, Institute for Basic Science (IBS), Ulsan 44919, Republic of Korea

3 School of Electrical and Electronic Engineering, Nanyang Technological University, 50 Nanyang Avenue, Singapore 639798, Singapore

4 Temasek Laboratories@NTU, 50 Nanyang Avenue, Singapore 639798, Singapore

5 Department of Chemistry, Ulsan National Institute of Science and Technology (UNIST), Ulsan 44919, Republic of Korea

6 School of Materials Science and Engineering, Nanyang Technological University, 50 Nanyang Avenue, Singapore 639798, Singapore

[†]These authors are equal major contributors to this work.

*e-mail: zhlee@unist.ac.kr; htteo@ntu.edu.sg

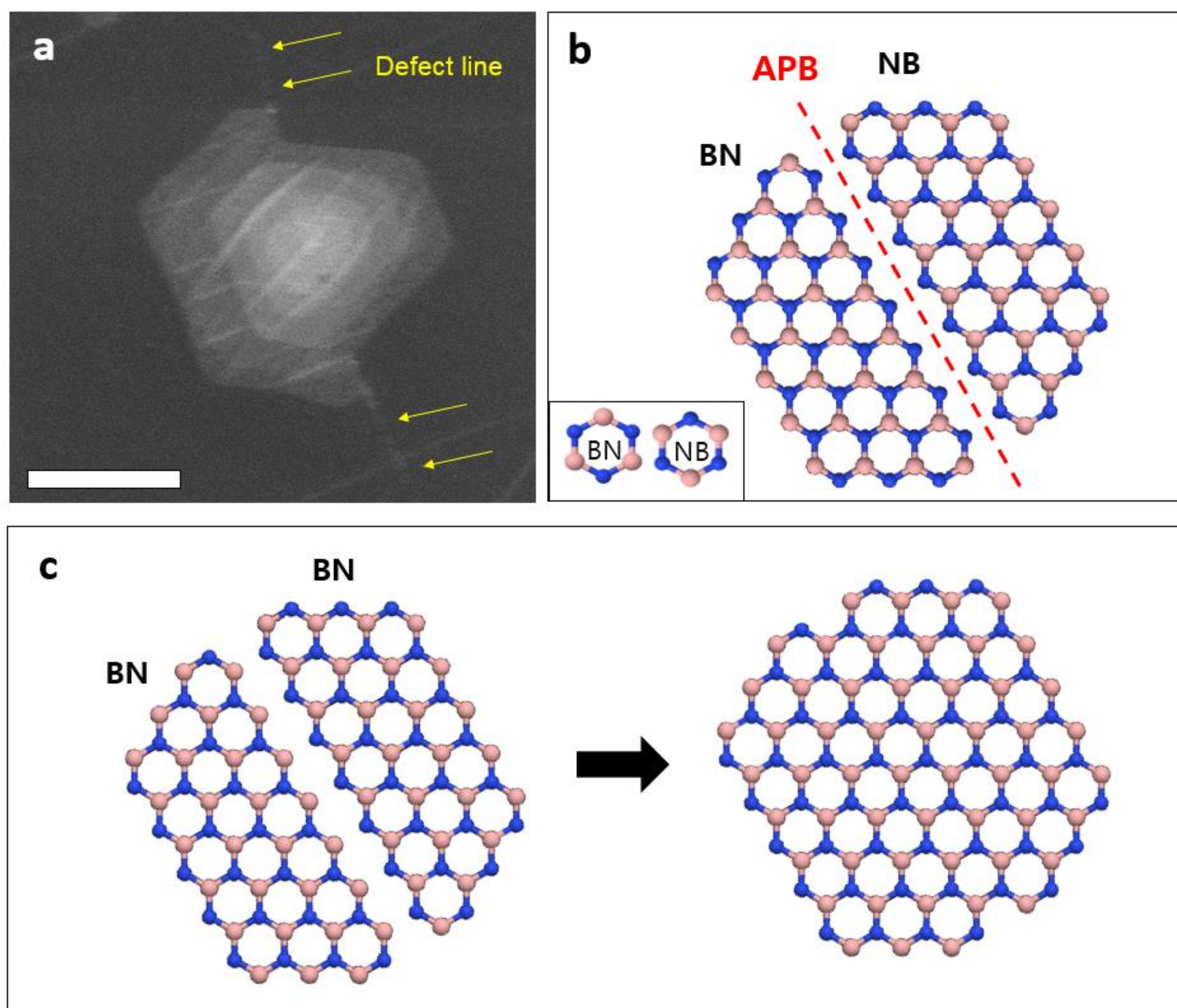

Figure S1. Multilayer h-BN islands grown along defect lines. h-BN single crystals have two orientation; BN and NB, which is 60 degree rotated (Refer to inset of (b)). Contrast to seamless stitching of BN/BN (or NB/NB) domains (c), coalescence of BN/NB domains leaves defect line. The boundary of BN/NB is called anti-phase boundary (APB). Scale bar, 1μm.

1. Demonstration of top growth of h-BN spirals

We experimentally demonstrated that h-BN spiral islands grow upward from the Cu substrate by comparing the orientations of triangular defects on each side of domains to APB (Figure S2). This demonstration is possible due to the characteristic behavior of h-BN defect growth under an 80 kV electron beam. (1) Under an 80 kV electron beam, atoms are knocked out leaving an N-terminated triangular hole defect[1-3]. Hexagonal hole defects with B-terminated edges can be created at elevated temperature[4] or at higher current density[5], but in our TEM image condition it is confirmed that N-terminated triangular hole defects are always created with TEM image simulations using MacTempasX[3]. (2) Since h-BN has an AA′ stacking structure, the orientation of the triangular defects are rotated 180 ° between layers (refer to the schematic in Figure 1e). (3) Atoms are normally ejected from the bottom layer first, and the triangular defects grow layer by layer. Therefore, the smallest triangular defects are found in the top layer[6]. Based on these characteristics of electron beam-induced h-BN defects, triangular defects for both top and bottom growth are illustrated in Figure S2. Note that the h-BN layers are turned upside down when transferred onto the TEM grid (Figure S2a) by a direct transfer method[7]. Figure S2A and B show the features of the triangular defects corresponding to top and bottom growth, respectively, including the layer boundary of the double layer and trilayer, for a comparison of the orientation of the triangular defects in the AR-TEM image in Figure S2d. As illustrated in Figure S2b,c, the orientations of the smallest triangular defect on the left and right of the layer boundary should be the same as that in the case of top growth and opposite in the case of bottom growth. In Figure S2d (taken a few seconds after Figure 1c), the empty regions with no atom contrast after the top layer is etched out are marked as purple triangles. The orientations of the purple triangles over the layer boundary are the same, which proves the top growth of h-BN layers. There are

exceptions such as small vacancies possessing the opposite orientation to the others like the green triangle marked in Figure S2d because of sputtering caused by the large momentum transfer so atoms exit the surface in the forward direction, but this is very rare.

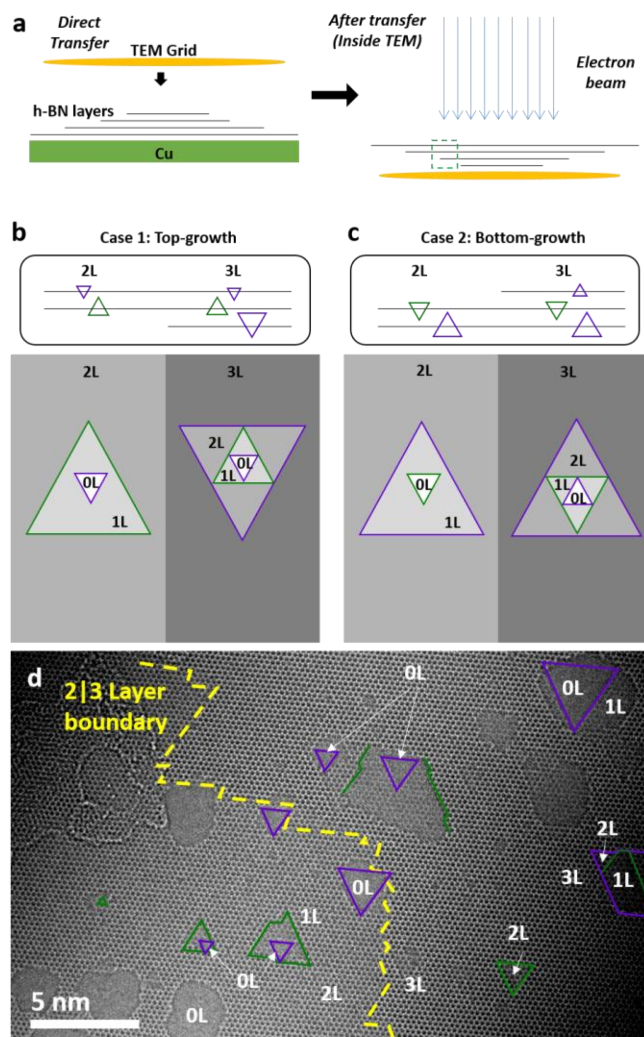

Figure S2. Top growth of h-BN spirals. (a) Schematic of multilayer h-BN grown upward from the Cu substrate. The h-BN layers are turned upside down after being transferred onto the TEM grid. (b, c) Schematic showing the features of triangular defects for top growth (b) and bottom growth (c). (d) AR-TEM image with triangular holes formed by prolonged electron beam irradiation. The image shows the area indicated by a red box in Figure 1b and corresponds to the area indicated by a green dashed box in (a). Scale bar, 5 nm.

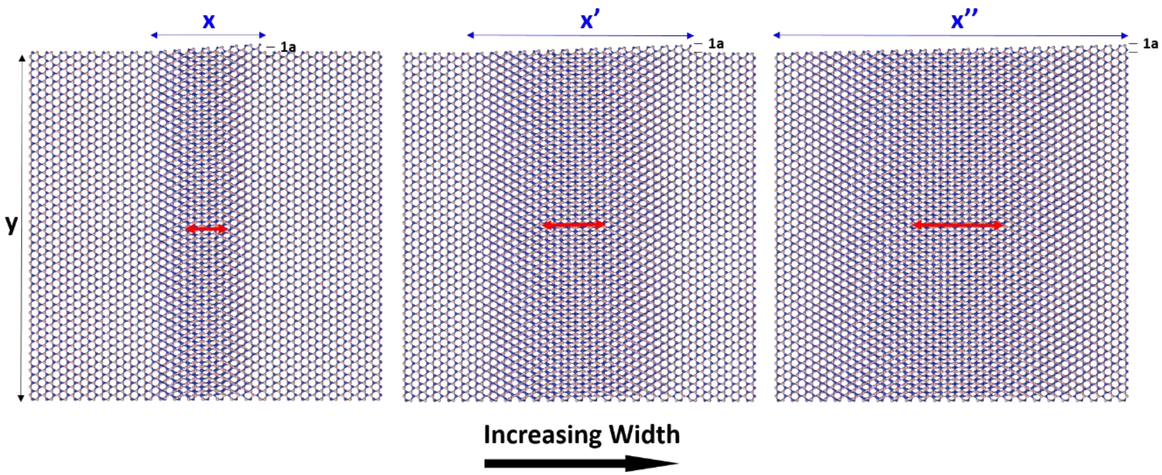

Figure S3. Relation between width of sheared region and the width of the square lattice region. "x" is the width over which shear is applied in the h-BN bilayer with fixed shear strength of 1 h-BN unit cell (2.50 Å) in the y-direction. The red arrows indicate the square lattice region resulting from shear. Larger "x" results in a wider region.

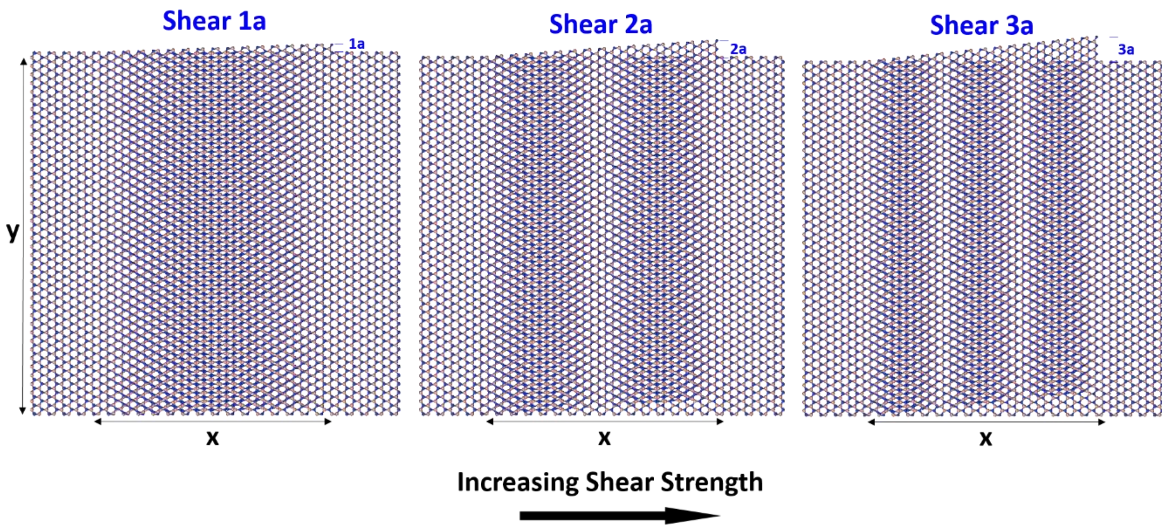

Figure S4. Relation between shear strength and the periodicity of the square lattice region. The periodicity of region increases per 1 h-BN unit cell (2.50 Å) of shear strain in the y-direction. The width of the sheared region (x) is fixed for the three models.

2. Theoretical analysis of shear strain band

2-1. Deduction of width of shear strain band

In the most stable configuration of h-BN (i.e., AA′ stacking), shear causes elastic deformation and the formation of other stacking sequences. Therefore, the increase in total energy is comprised of two parts: the change in elastic deformation energy (ΔE_{ED}) and the change in van der Waals interaction (ΔE_{vdW}) between adjacent h-BN layers.

$$\Delta E_{total} = \Delta E_{ED} + \Delta E_{vdW} \quad (1)$$

ΔE_{ED} can be expressed as follows:

$$\Delta E_{ED} = G \times (a/b)^2 \times (h \times b \times a), \quad (2)$$

where G is the shear modulus, a is the length of the displacement of h-BN along the zigzag direction, b is the width of the shear strain band in the armchair direction, and h is the layer distance in h-BN. Thus, (a/b) is the shear strain and $(h * b * a)$ is the effective volume of the sheared material (see Figure S5).

The increase of total energy resulting from the vdW term (ΔE_{vdW}) could be written as:

$$\Delta E_{vdW}\Delta E_{vdW} = \alpha * b * a, \quad (3)$$

where α is the scaling factor, which is equal to the reduction in vdW energy per area.

Thus, ΔE_{total} can be obtained as follows:

$$\Delta E_{total} = G * a^3 * h/b + \alpha * a * b. \quad (4)$$

ΔE_{total} is minimized when $\frac{\partial \Delta E_{total}}{\partial b} = 0$. Therefore, the width of the sheared region at equilibrium can be expressed as follows:

$$b_{eq} = (G * h/\alpha)^{1/2} * a. \quad (5)$$

To calculate b_{eq}, the shear modulus G and the scaling factor α are estimated theoretically, as detailed in the following section.

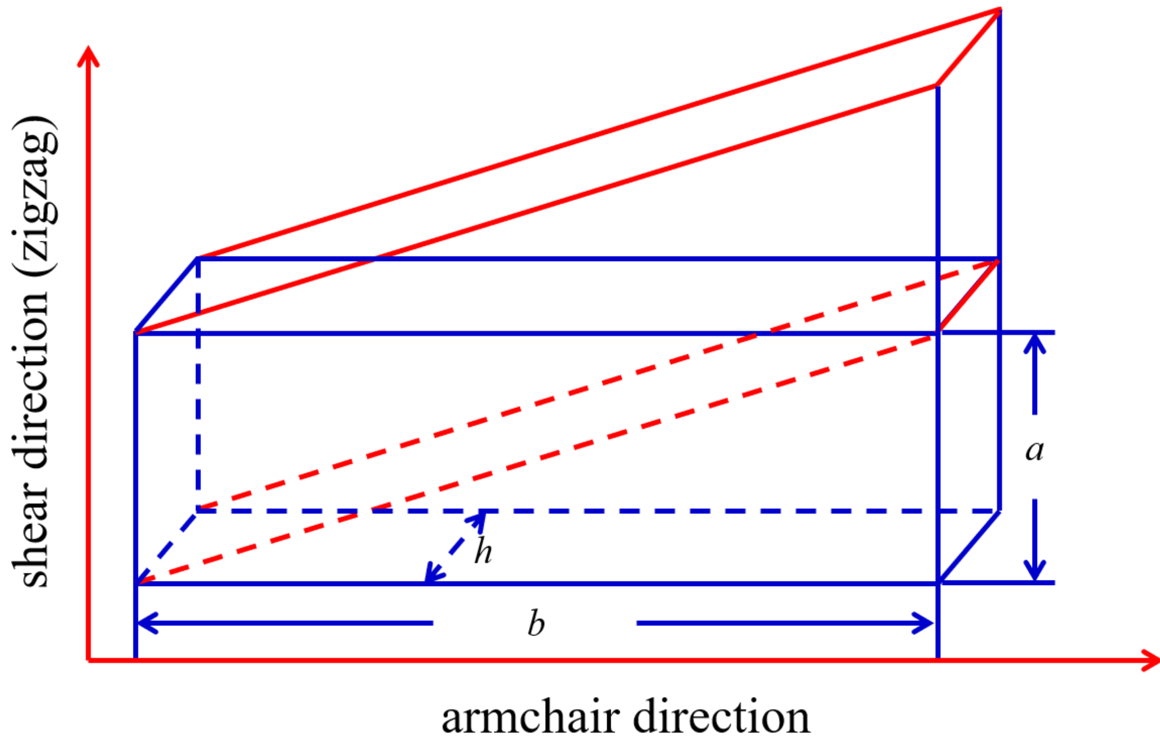

Figure S5. Theoretical model used to calculate the increase in total energy caused by shear strain in *h*-BN.

2-2. Theoretical estimation of *G*

We obtained *G* using the definition in Eq. (2). Four different supercells of h-BN were designed. The lattice constants are listed in Table S1. All supercells had same *a* and *h* but different *b* because they had different periodic units along the armchair direction. Shear was imposed along the zigzag direction with a displacement of 2.50 Å, which is equal to *a*. The value of *h* was set as the interlayer distance of h-BN (3.40 Å). By only adjusting *b*, we obtained different values of ΔE_{ED} using DFT calculations and determined the average value of *G* to be 1036.48 meV/Å^3.

Table S1. Lattice constants and shear modulus for the chosen supercells.

Supercell		I_1	I_2	I_3	I_4
Lattice constant (Å)	*a*	2.50	2.50	2.50	2.50
	b	17.33	25.99	34.65	43.32
Shear modulus (meV/Å^3)		1026.66	1036.74	1040.19	1042.34
Average shear modulus (meV/Å^3)		1036.48			

2-3. Theoretical estimation of *α*

The scaling factor *α* represents the increase in energy per area caused by the reduction in the vdW interaction between adjacent h-BN layers. To calculate *α*, we designed a bilayer h-BN containing a total of four N atoms and four B atoms. The volume of the supercell was 2.50 × 4.33 × 20.00 $Å^3$. The bottom layer was fixed, and the atoms in the top layer were slid in 0.1 Å steps until the distance was of a full h-BN unit cell, 2.50 Å along the zigzag direction. The relation between the step distance and ΔE_{vdW} is shown in Figure S6.

The value of *α* can then be estimated as the average of the vdW energy difference with the step distance:

$$\alpha = \frac{\sum \Delta E_{vdw} * \Delta x}{\sum \Delta x} = 2.41\ \mathrm{meV/Å^2}. \quad (6)$$

The dependence of ΔE_{total}, ΔE_{ED}, and ΔE_{vdW} on the width of the sheared region are shown in Figure S6. Having obtained *G* and *α*, *b* in the equilibrium state can be estimated as follows:

$$b_{eq} = (\alpha \times h/\alpha)^{1/2} \times a = 95.6\ Å = 9.56\ \mathrm{nm}. \quad (7)$$

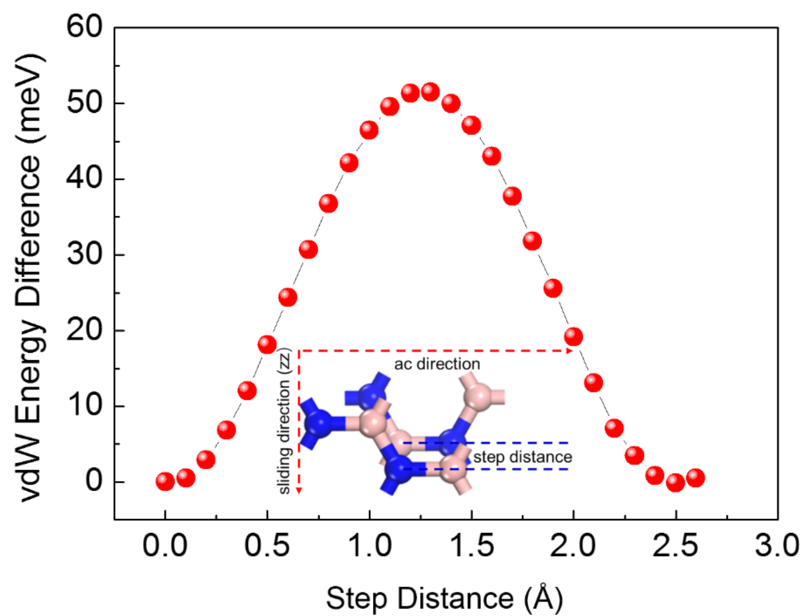

Figure S6. Relation between the van der Waals (vdW) energy difference and step distance. The step increment is 0.1 Å. The inset shows the model used to calculate α.

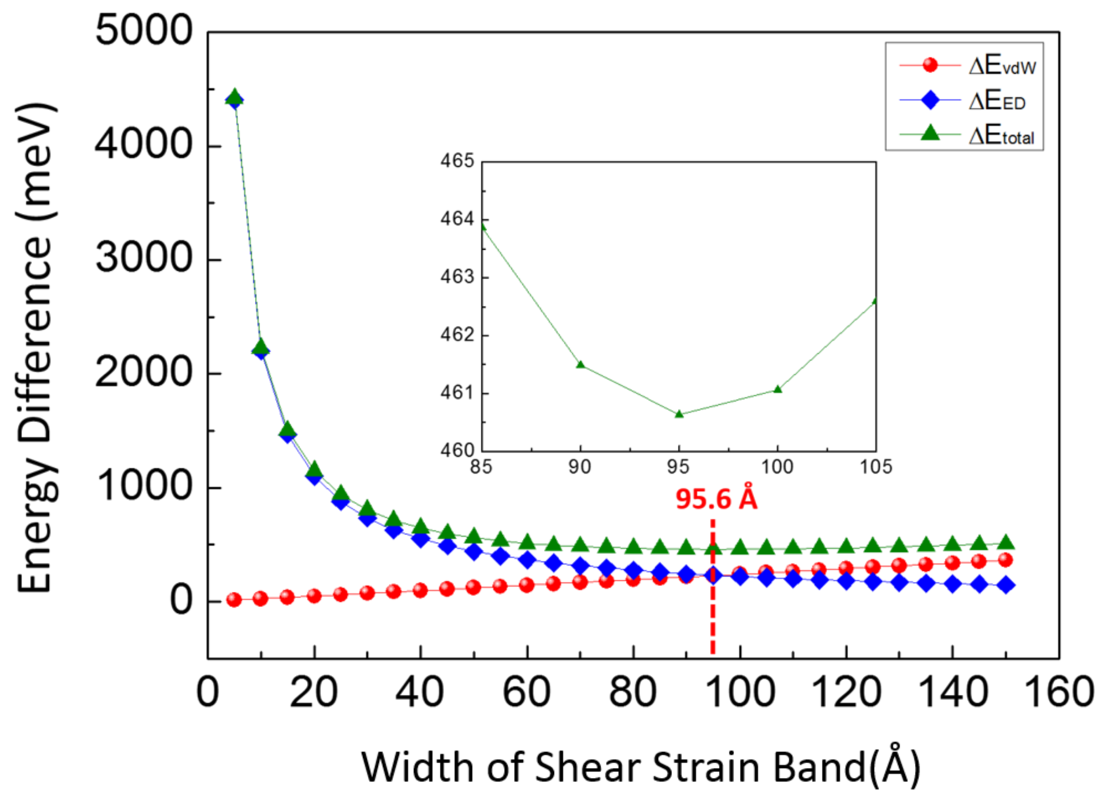

Figure S7. Dependences of ΔE_{total}, ΔE_{ED}, and ΔE_{vdW} on the width of the shear strain band. ΔE_{total} is minimized at a width of 9.56 nm. The energy difference is magnified in Figure 4f.

References

1. Yin, L. C.; Cheng, H. M.; Saito, R. *Phys. Rev. B.* **2010,** 81, (15).
2. Kotakoski, J.; Jin, C. H.; Lehtinen, O.; Suenaga, K.; Krasheninnikov, A. V. *Phys. Rev. B.* **2010,** 82, (11).
3. Ryu, G. H.; Park, H. J.; Ryou, J.; Park, J.; Lee, J.; Kim, G.; Shin, H. S.; Bielawski, C. W.; Ruoff, R. S.; Hong, S.; Lee, Z. *Nanoscale* **2015,** 7, (24), 10600-10605.
4. Pham, T.; Gibb, A. L.; Li, Z. L.; Gilbert, S. M.; Song, C. Y.; Louie, S. G.; Zett, A. *Nano Lett* **2016,** 16, (11), 7142-7147.
5. Gilbert, S. M.; Dunn, G.; Azizi, A.; Pham, T.; Shevitski, B.; Dimitrov, E.; Liu, S.; Aloni, S.; Zettl, A. *Sci Rep-Uk* **2017,** 7.
6. Meyer, J. C.; Chuvilin, A.; Algara-Siller, G.; Biskupek, J.; Kaiser, U. *Nano Lett* **2009,** 9, (7), 2683-9.
7. Regan, W.; Alem, N.; Aleman, B.; Geng, B. S.; Girit, C.; Maserati, L.; Wang, F.; Crommie, M.; Zettl, A. *Appl. Phys. Lett.* **2010,** 96, (11).